Toward In-Situ Sensing of Powder Bed Packing Density in Metal Binder Jetting via Recoating-Force and Acoustic Signals: A Comparison

Chen Qian , Alexander Martinez-Marchese , Chinedum Okwudire *

Posted Date: 23 April 2026

doi: 10.20944/preprints202604.1606.v1

Keywords: additive manufacturing; in-situ monitoring; binder jetting

 doi:10.20944/preprints202604.1606.v1

Article

Toward In-Situ Sensing of Powder Bed Packing Density in Metal Binder Jetting via Recoating-Force and Acoustic Signals: A Comparison

Chen Qian, Alexander Martinez-Marchese and Chinedum Okwudire *

Department of Mechanical Engineering, University of Michigan, Ann Arbor, MI 48109 USA
* Correspondence: okwudire@umich.edu

Abstract

Metal binder jetting (MBJ) is an additive manufacturing (AM) process that offers advantages such as high speed, low cost, and low residual stress, compared to the prevalent fusion-based metal AM methods. However, a major barrier to MBJ is the low density of manufactured parts, which restricts part quality and limits its applications. One key process parameter that affects part density is the packing density of the powder bed. In general, a higher packing density is preferable in MBJ. Although research has been conducted to enhance the packing density ex-situ, most proposed approaches lack robustness when applied to real-world printing, where environmental variations and stochastic powder behavior introduce inconsistencies. An in-situ sensing method for packing density can mitigate these issues in several ways. It enables the implementation of feedback control strategies to regulate packing density during printing, contributes to comprehensive in-situ process monitoring, and provides quantitative data to support post-processing analysis and optimization. However, effective in-situ methods for accurately sensing packing density remain limited. To fill this research gap, two methods, namely ultrasound (acoustic) and recoating-force sensing, are proposed as potential approaches for in-situ sensing of powder packing density. Using a dedicated test platform, their responses to different powder bed packing densities are measured and compared. The results show a strong correlation between packing density and the sensor measurements, with differing levels of estimation confidence, demonstrating promising potential for their implementation as in-situ packing density sensors. Furthermore, the concept of sensor fusion is tested by combining the force-sensing and acoustic-sensing data, leading to improvements in the estimation confidence.

Keywords: additive manufacturing; in-situ monitoring; binder jetting

1. Introduction

Binder jetting (BJ) is an additive manufacturing method that uses a print head to selectively deposit binder droplets onto a powder bed, bonding the particles layer by layer to form parts. Specifically, metal binder jetting (MBJ) aims to fabricate solid metal parts by adopting metal powder as the printing material. As shown in Figure 1, MBJ starts with a printing stage, which involves: (a) Spreading a thin layer of powder on the build plate, followed by (b) using an inkjet printhead to dispense binder ink agent on the powder layer. Then, optionally, (c) mildly heating the powder layer to dry the binder, and then lowering the powder bed. Steps (a) to (c) are repeated in the subsequent layers until the parts are fully finished. Steps (d) to (f) show the steps for post-processing after the printing is finished. The printbed is initially (d) sent to a curing oven, heated to temperatures sufficient to solidify the binder agent, allowing the green parts to be removed from the powder bed securely. Then (e) the powder is removed, and the green parts are carefully extracted from the powder bed. Finally, (f) the green parts are transferred to a sintering furnace and are sintered with a pre-defined temperature profile to remove the binder ink and form solid metal parts.

 doi:10.20944/preprints202604.1606.v1

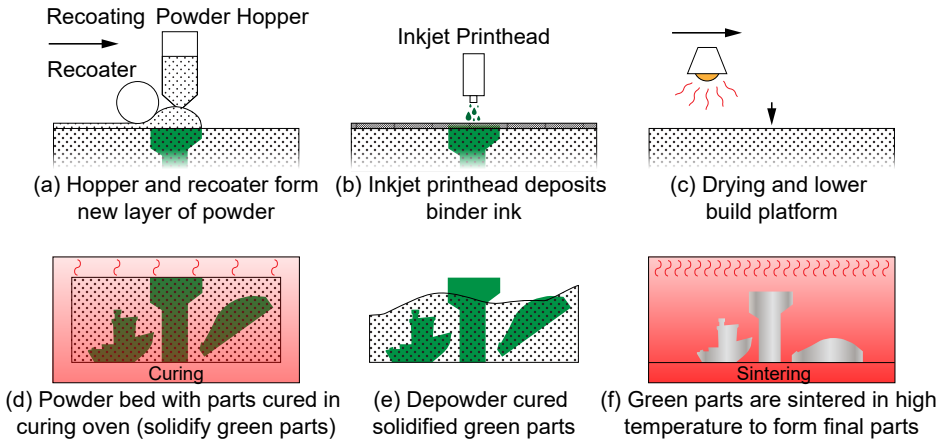

Figure 1. Metal binder jetting (MBJ) 3D printing process.

MBJ has been shown to offer multiple advantages over the prevailing fusion-based metal AM methods, like laser powder bed fusion (LPBF), electron-beam powder bed fusion (EBPF), and directed energy deposition (DED). Similar to conventional 2D printing, MBJ uses inkjet printheads to rapidly deposit binder onto the powder bed and form 2D patterns almost instantly. In contrast, other aforementioned AM techniques rely on a focused energy source to locally heat and solidify the metal, requiring a planned scanning path to move the energy source across parts layer-by-layer, which makes the printing time grow rapidly as a function of the number and size of parts. In MBJ, the time for each layer is much less dependent on the number and size of parts on the build platform, making it more advantageous in terms of printing speed [1–3] and scalability [4–6]. Furthermore, the post-processing steps (that include curing and sintering) heat up and cool down the parts uniformly, creating negligible residual stress in the final printed parts [1,2,7]. Most of the post-processing steps can be done as a batch operation, which further reduces the cost, and leads to additional speed advantages for MBJ [8].

Despite the multiple advantages of MBJ, literature shows that parts printed with MBJ tend to have lower final part density compared to other AM techniques [3,6,9], affecting the strength of the printed parts and limiting MBJ's applications [10]. One of the reasons that contributes to this reduced printing quality is the low powder bed packing density in the MBJ process [6,10]. Powder bed packing density α (also known as packing fraction) is a critical process parameter in MBJ. It is the quotient of the bulk density ρ_b (i.e., the density of the powder particles including the pores between them) and the solid density ρ_s (i.e., the density of the same material as the powder, without pores) [11], as shown in Figure 2. A lower packing density indicates more pores are present in the powder bed. Since the pores cannot be completely eliminated during the sintering process [6,12], more pores in the powder bed (i.e., lower packing density) can lead to poorer MBJ printing quality. Literature shows that the packing density has a positive correlation with multiple printing quality indices, including the porosity, shape distortion, and mechanical strength of printed parts [10,12,13].

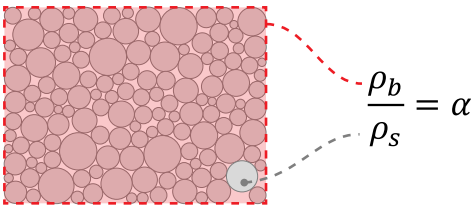

Figure 2. Calculation of powder bed packing density α.

Several studies have been carried out, and methods have been proposed to improve packing density in MBJ. The methods often involve *ex-situ* calibration of powder properties or printing process parameters. For example, Bai et al. [14], Du et al. [15], Yang et al. [16] and Chen et al. [17] show that

 doi:10.20944/preprints202604.1606.v1

bimodal and multi-modal powder can enhance packing density and therefore improve the printed parts' quality. Lee et al. [18] and Barthel et al. [19] utilized simulation and experimental approaches to study the recoating parameters in roller-based MBJ systems, including roller transverse and rotational speeds, layer thickness, roller diameter, and the effects of the supply-to-spread ratio on the packing density. They found that lower roller transverse speed and layer thickness, and larger roller diameter improved the powder packing density. In a similar vein, Lee [20] and Cao [21] et al. found that using a counter roller for recoating could improve packing density. Although these approaches offer significant insights, the experiments are typically conducted with fixed process parameters for the entire build, which limits their ability to address localized powder bed defects. As a result, they often lack robustness under real-world printing conditions, where variations in the printing process and the stochastic nature of powder behavior introduce local inconsistencies. These local inconsistencies can have significant downstream consequences. As an example, Paudel et al. shows that the local packing density variations in large part will affect the shape distortion prediction during post-processing with FEM simulation, and this can potentially affect the distortion-correction in MBJ[22]. Several factors contributes to the emergence of these local packing density consistencies. For example, binder–powder interaction is a factor that can affect powder bed packing quality [23,24]. Since binder deposition varies layer by layer, it may introduce variations between layers due to differences in the deposition pattern. Another example is that, for cost-effectiveness of the process, recycled powder and cheaper water-atomized powder are sometimes used in MBJ. Compared to commonly used gas-atomized and plasma-atomized virgin powder, water-atomized and recycled powder contain more irregularly shaped particles and change the powder size distribution, leading to poor packing density [25–29].

The aforementioned limitations of the existing approaches for improving packing density underscore the need for an in-situ sensing method that can capture the powder packing anomalies during printing. First, an in-situ sensing approach enables the implementation of closed-loop control strategies by providing real-time information about the powder bed state. Based on this information, appropriate actuation can be applied to mitigate packing anomalies during printing, thereby achieving more uniform packing and improving part density and homogeneity. Second, in-situ measurement offers a low-cost means of estimating part density immediately after printing, without requiring additional post-printing characterization. The measured packing density can subsequently support post-processing analysis and parameter optimization such as [22].Third, in-situ packing density measurement can serve as a complementary signal within broader in-situ quality monitoring frameworks, enhancing the overall robustness and reliability of process control. However, most of the existing approaches for measuring packing density are *ex situ*. The standard approach involves printing fixed-volume density cups and measuring the mass of powder inside to calculate the packing density [30–33]. Alternatively, Ali et al. explored the use of micro-computed tomography (μCT) to construct the 3D image of samples collected from the powder bed and measure packing density *ex situ* [34].

Some researchers have demonstrated potential approaches to measure the packing density *in situ*. For example, some researchers used X-ray imaging to monitor the binder jetting 3D printing process [24,35–37], enabling viewing of the powder bed's internal structure in real-time. However, X-ray imaging is expensive, poses safety risks, and has limited penetration depth with metal powder. Measuring the powder bed surface morphology (via 3D scanning) has also been explored as a proxy for sensing packing density *in situ* [38–44]. Because surface morphology reveals visible pores and defects on the powder bed, it offers partial insight into the overall packing condition. Researchers have further quantified this by analyzing surface roughness as an indicator of packing quality [37,45,46]. While surface morphology can be measured *in situ* [38–42], it is inherently limited to surface-level features and does not account for subsurface voids. Recent work has explored the use of infrared thermography for sensing packing density *in situ* [47–50]. However, while it is capable of accurately estimating packing density, infrared thermography relies on the slow thermal response of the powder bed. As a result, it requires a long waiting period after each layer and is sensitive to convection, reducing its responsiveness and reliability [47].

 doi:10.20944/preprints202604.1606.v1

To address the identified research gap in *in-situ* measurement of packing density in MBJ, this paper and its preliminary conference version [51], make the following original contributions to the literature:

- It proposes the use of recoating force as an *in-situ* sensor for packing density. It achieves this by measuring the vertical reaction force from the powder bed during the recoating process and using the force as a proxy for packing density.
- It proposes the use of acoustic signals for *in-situ* sensing of packing density. This method utilizes the intensity of ultrasound signals reflected from a powder bed to deduce the bed's acoustic impedance, which is correlated with packing density.
- It experimentally compares the aforementioned two sensing approaches, using a specially designed testbed, to highlight their strengths and weaknesses, and how they can be combined to achieve better sensing outcomes.

The remainder of this paper is organized as follows. Section 2 presents the rationale behind the proposed force-sensing and acoustic-sensing methods. Section 3 describes the materials and experimental methods used in this study. The results and discussion are provided in Section 4. Finally, Section 5 summarizes the conclusions and outlines directions for future research.

2. Rationale for the Proposed Sensing Methods

2.1. Force-Sensing Method

In metal binder jetting (MBJ), a recoating system spreads and compacts a layer of powder prior to binder deposition. We hypothesize that the vertical component of the reaction force exerted on the recoater during this recoating process is positively correlated with the powder bed packing density. As the recoater advances, it deforms the powder bed and generates reaction forces that reflect the mechanical response of the compacted layer. In Figure 3, the vertical and horizontal components of these reaction forces are labeled as F_v and F_h, respectively. We believe that F_v, the vertical component of this reaction force, analogous to the reaction force when compressing a set of parallel springs in the vertical direction, has a positive correlation with the powder bed stiffness. As a result, variations of powder bed packing density lead to changes in the stiffness and thereby alter the vertical force exerted on the recoater.

Because recoating architectures vary across commercial systems, it is important to clarify how this hypothesis applies under different configurations. Some platforms employ multi-stage recoating systems, such as the TripleACT system [52], in which a coarse roller first establishes a uniform layer height, followed by a compaction roller that determines the final packing density. In such systems, the reaction force acting on the final compaction roller can be associated with the stiffness of the compacted powder bed and is therefore expected to correlate with packing density.

However, directly integrating a force-sensing function into existing rollers may necessitate intrusive structural modifications, which are undesirable in commercial machines. In such cases, a detachable force-sensing recoater can be introduced as an auxiliary module positioned downstream of the primary spreading element. With this configuration, the auxiliary recoater serves as a functional analog to a compaction recoater, allowing the vertical reaction force associated with the compacted powder bed to be measured. Consequently, the proposed force-packing density relationship can be inherently examined in both augmented single- or multi-stage systems for experimental evaluation.

In the present study, this concept is emulated experimentally by preparing pre-compacted, uniform powder beds and subsequently recoating them using a recoater instrumented with force sensors. Under this configuration, the relationship between recoating force and packing density, before and after recoating, can be quantitatively evaluated.

 doi:10.20944/preprints202604.1606.v1

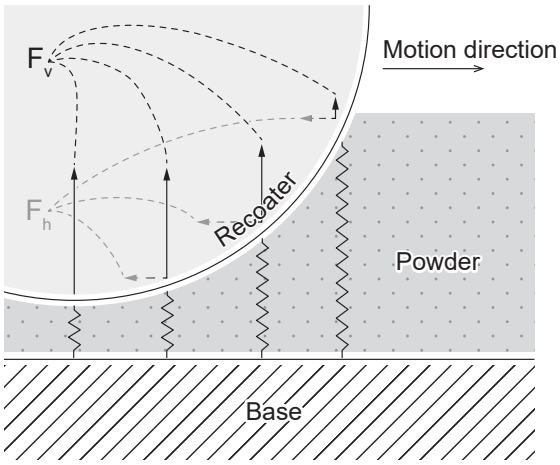

Figure 3. The spring system assumption for recoating force, where F_h and F_v respectively represent the horizontal and vertical reaction forces on the recoater.

2.2. *Acoustic-Sensing Method*

The acoustic sensing method utilizes an ultrasonic transducer to quantify packing density based on the intensity of the reflected acoustic signal. Al-Lashi et al. [53] demonstrated that when an ultrasound wave travels from air to a powder surface, the reflection coefficient Γ, defined as the ratio of the intensity of the reflected signal $I_{r,p}$ to that of the incident signal I_i, can be calculated by Equation (1).

$$\frac{I_{r,p}}{I_i} = \Gamma = \frac{Z_p - Z_a}{Z_p + Z_a} \tag{1}$$

Here, Z_a and Z_p are the acoustic impedances of air and powder, respectively. A graphical illustration of this reflection process with parameters highlighted is provided in Figure 4.

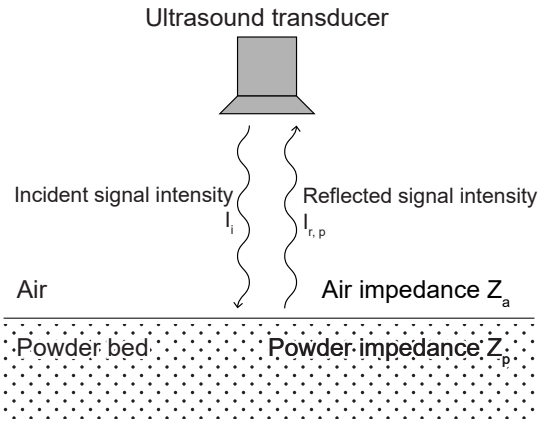

Figure 4. Graphical illustration of using acoustic-sensing method to detect the powder packing density.

Assuming the impedance of air Z_a and intensity of incident signal I_i are constants, the reflection coefficient is primarily influenced by the acoustic impedance of powder. The acoustic impedance of powder is given by Equation (2) [53]

$$Z = \rho_b c_p \tag{2}$$

where ρ_b is the bulk density of powder and c_p is the propagation speed of sound in the powder. Literature has shown that the c_p is density-dependent [54], and that acoustic impedance is dependent on ρ_b as well [55]. Packing density of powder α is the ratio of the powder's bulk density ρ_b to the density of the solid material ρ_s, as shown in Equation (3):

$$\alpha = \frac{\rho_b}{\rho_s} \tag{3}$$

 doi:10.20944/preprints202604.1606.v1

Therefore, packing density has a linear correlation with powder density. Hence, changes in packing density alter the powder's acoustic impedance, thereby affecting the reflection coefficient Γ, which can be detected by acoustic sensors.

3. Materials and Methods

To test the hypothesis behind each of the proposed sensing methods, a setup consisting of: (1) a powder preparation apparatus, (2) a force-sensing test apparatus, and (3) an acoustic-sensing test apparatus was designed and built. An optical table, serving as the ground, was used to mount the setup. Höganäs X-17-4 PH -30 µm water-atomized powder (WAP) was used for all the experiments. The physical properties of the powder are listed in Table 1. A scale (Torbal™AD3200, capacity: 3200 g, linearity: 0.02 g, Scientific Industries Inc., Bohemia, NY) was used to take the mass measurements.

3.1. Powder-Bed-Preparation Apparatus and Methodology

As shown in Figure 5a, a custom powder preparation apparatus (comprising a press, press guide, datum pad, and powder bed tray) was used to create powder bed samples with varying packing densities for testing both the force-sensing and acoustic-sensing methods. The powder bed tray is a CNC-milled 6061 aluminum component, measuring 100 × 100 × 25 mm^3 (length × width × height) externally, with an inner cavity of 60 × 60 × 18 mm^3 to contain the powder samples. The press is also machined from 6061 aluminum and features a black anodized finish. Its main body measures 60 × 60 × 60 mm^3 and includes a datum pad on its top surface that sits flush with the guide during compression. The press guide is a CNC-milled 6061 aluminum frame with a through-cavity matching the 60 × 60 mm^2 cross-sectional area of the press and powder bed cavity. It serves both to contain excess powder and to ensure vertical alignment during pressing. The datum pad, with a thickness of 100 µm, creates a height offset by the same amount between the powder bed surface and the top surface of the powder bed tray, as discussed further in Section 3.2.

Figures 5b–d illustrate the process of preparing the powder bed with controlled packing densities, using the powder-preparation apparatus. First, the press guide, datum plate, and powder bed tray are assembled together to form a container. Powder with a prescribed mass is then loaded into the assembled container. To ensure uniformity, an auxiliary leveling blade is used to preliminarily flatten the surface. Next, the press is inserted into the tray until the press reaches the bottom to compress the powder into the confined volume. By altering the powder mass loaded into the container, the packing density can be varied. Finally, the press, guide, and datum pad are removed. Due to the cohesion force of powder, the powder bed retains its shape, and the intended 100 µm height difference is preserved. The mass of powder remaining in the tray after compression is measured and used to calculate the pre-recoating packing density. Note that when the packing density is higher, a larger pressure is required to consolidate the powder into the tray. Here, for trials with packing densities larger than 0.505, we used a mallet to facilitate this process.

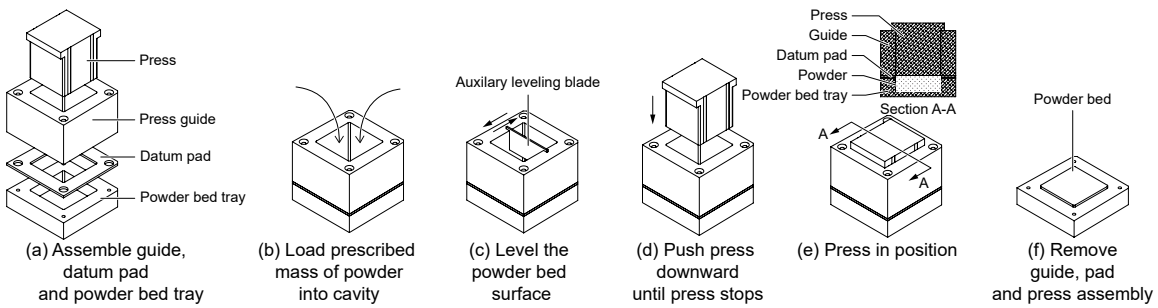

Figure 5. Step-by-step process for generating varying levels of packing density using the powder-bed-preparation apparatus.

 doi:10.20944/preprints202604.1606.v1

Table 1. Physical properties of Höganäs X-17-4 PH -30 µm water-atomized powder (WAP). Source: Höganäs X-17-4 PH -30 µm WAP certification of analysis.

D10	D50	D90	Apparent Density (Carney)	Tap Density
5.0 µm	14.1 µm	29.5 µm	3.13 g/cm^3	4.35 g/cm^3

3.2. Force-Sensing Apparatus and Methodology

Based on the hypothesis that the vertical recoating force is positively correlated with packing density, the force-sensing test apparatus shown in Figure 6a was built. The apparatus primarily consists of a recoater attached to a load cell, a linear stage, and the powder bed tray from Figure 5. The recoater is a non-rotating stainless steel cylinder of 5 mm diameter rigidly attached to the load cell. It has a polytetrafluoroethylene (PTFE) coating such that the outer diameter of the recoater, including the PTFE coating, is 7 mm. A load cell (a18112500ux0194, Uxcell, Hong Kong) with a range of 1.96 N and 5% full-scale accuracy is used in this apparatus. The centerline of the recoater is aligned with the centerline of the load cell to reduce the torsional effect introduced by the horizontal reaction force from the powder bed. The linear stage used in this research consists of a ball screw (BSST1505-473-RLC, Misumi USA, Schaumburg, IL) and a servo motor (SGMAH-02F4C2, Yaskawa America Inc., Rochester Hills, MI). The powder bed tray used in this test is described in Section 3.1. A servo motor driver (Soloist CP-10, Aerotech Inc., Pittsburgh, PA) and a load cell amplifier (1046_1, Phidgets Inc., Calgary, AB, Canada) are connected to MATLAB, enabling the linear drive to be commanded and data to be collected for the experiments.

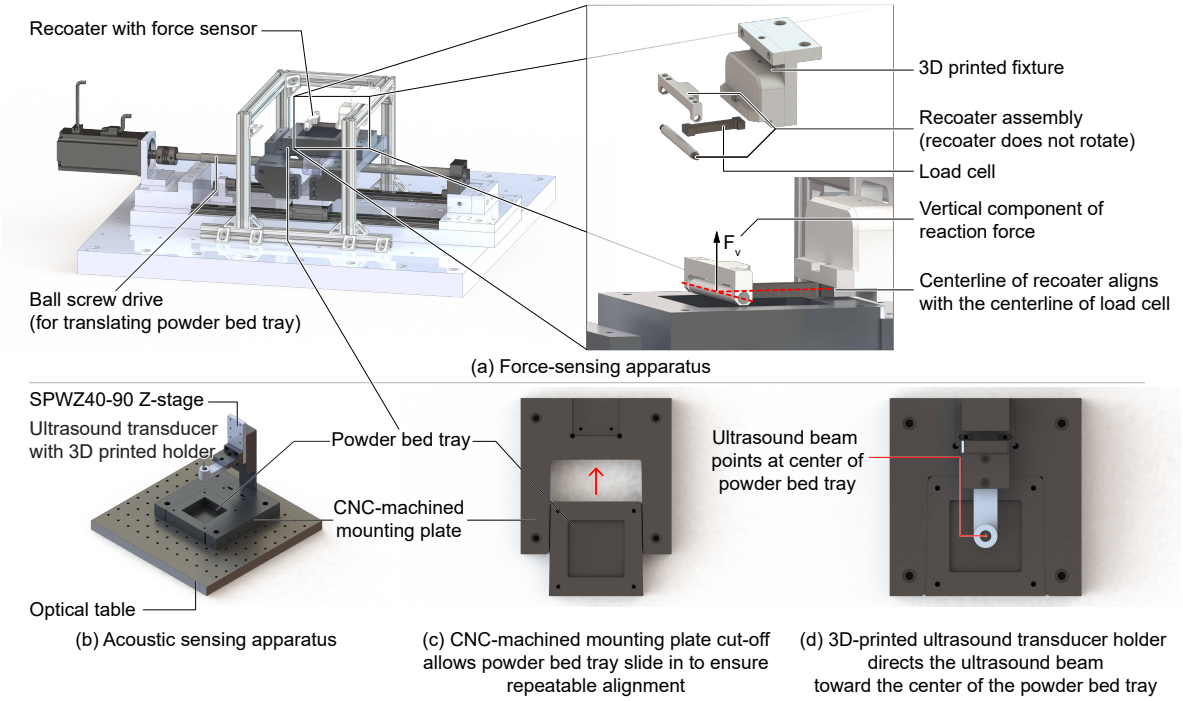

Figure 6. Illustration of force-sensing and acoustic-sensing apparatuses. Note that the same powder bed tray from Figure 5 is used in both apparatuses.

We imitate the recoating process in MBJ by commanding the linear stage to drive the powder bed tray at a constant speed to level the powder surface. This process replicates the powder compaction behavior of multi-stage powder spreading systems and the augmented recoating configuration described in Section 2.1. A speed of 15 mm/s was chosen for all of the experiment trials conducted. This value falls within the operational range reported in prior binder jetting studies and corresponds to stable spreading conditions in the present system configuration [56,57]. The powder bed surface was prepared to be 100 µm higher than the powder bed tray's surface, allowing the recoater to level the powder surface and achieve powder bed compaction. The recoater's height and the powder bed's

 doi:10.20944/preprints202604.1606.v1

orientation were adjusted such that the recoater's bottom surface was just in contact with the powder bed surface at both the leading and trailing rims of the powder surface. During this process, the load cell recorded the vertical reaction force from the powder bed.

3.3. Acoustic-Sensing Apparatus and Methodology

The apparatus for acoustic sensing is shown in Figure 6(b). It contains a fine manual linear Z-stage (SPWZ40-90, China) for positioning the ultrasound transducers. The stroke, resolution, and parallelism of the stage are respectively ±30 mm, 0.01 mm, and 0.06 mm. The same powder bed used in 3.2 for force sensing is used for the acoustic-sensing experiments in order to get comparative results. A CNC-machined mounting plate (made of 6061 Aluminum Alloy) is used to mount the Z-stage on the optical table. The mounting plate features a cutout that allows the powder bed tray to slide in from the side, as shown in Figure 6c. This ensures repeatable alignment and easy insertion/removal, thus preventing the introduction of disturbances to the powder bed during testing.

Following [53,58], two ultrasound transducers with 100 kHz and 200 kHz operation frequencies (respectively model # H2KA200KA1CD00 and H2KA100KA1CD00 from Unictron Technologies Corp., Taiwan) were used in our experiments. The transducers were mounted to the Z-stage using 3D-printed holders made of acrylonitrile butadiene styrene (ABS), each aligned to direct the ultrasound beam toward the center of the powder bed tray, as shown in Figure 6d. A square wave pulser/receiver (5077 PR, Olympus Corp., Tokyo, Japan) was used to generate the signal to drive the ultrasound transducer and amplify the reflected signals. The reflected signals were then collected by an oscillator (DSOX1102A, Keysight Technologies Inc., Santa Rosa, CA). In addition to the directly reflected signals, the receiver also detected echo signals from reverberations of the acoustic waves. The distances between the ultrasound transducers and the powder bed surface were adjusted to ensure that the reflected and echo signals were sufficiently separated temporally, so that they could be isolated from each other. This enabled the reflected signals to maintain strong intensity, thereby yielding high resolution. The distances were set to 130.4 mm and 59.4 mm for the 100 kHz and 200 kHz ultrasound transducers, respectively. The receiver gain of Olympus 5077PR was adjusted to be 25 dB and 35 dB for the 100 kHz and 200 kHz ultrasound transducers, respectively. Both ultrasound transducers were driven by 400 V pulses.

3.4. Experiment Design and Process

To ensure that the results from force-sensing and acoustic-sensing could be fairly compared to each other, the test sequence shown in Figure 7 was used for each trial. The sequence involves five steps:

(a) Prepare the powder bed with controlled density, then measure the mass inside the powder tray to calculate the pre-recoating packing density.
(b) Install the powder bed on the acoustic-sensing apparatus and collect the pre-recoating acoustic response data using the ultrasound transducer.
(c) Install the powder bed on the force-sensing apparatus, then perform the recoating process to collect the vertical reaction force signals.
(d) Install the powder bed tray on the acoustic-sensing apparatus again and collect the post-recoating acoustic response data using the ultrasound transducer.
(e) Measure the mass of powder left inside the powder bed tray to calculate the post-recoating packing density.

Note that after the recoating, some residual powder may remain on the rims of the powder bed tray, as shown in Figure 8a. Between steps (c) and (d) in Figure 7, the residual powder is carefully cleaned, as shown in Figure 8b.

 doi:10.20944/preprints202604.1606.v1

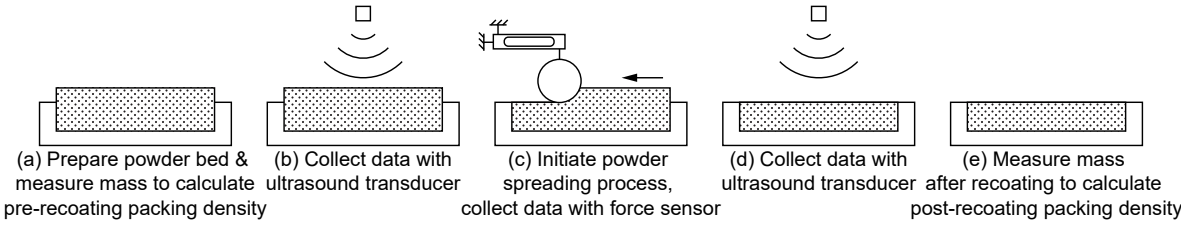

Figure 7. Test sequence for each trial comprising the force-sensing and acoustic-sensing methods.

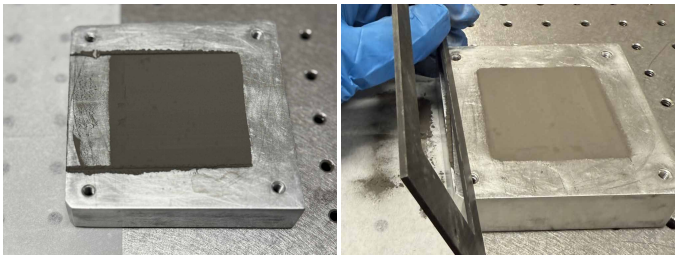

Figure 8. Residual powder on rim is cleaned between step (c) and (d) in Figure 7.

For the acoustic-sensing methodology, since two ultrasound transducers were tested, switching between them required retuning both the Z-stage height and the square wave pulser/receiver after each switch, which risked introducing lots of human error. To minimize the number of switches, we first conducted 40 experimental trials using the 100 kHz ultrasound transducer. Then we switched to the 200 kHz transducer, configured the acoustic-sensing apparatus for the 200 kHz transducer, and conducted another 40 trials with the 200 kHz transducer. This experimental arrangement ensured that only one transducer switch was needed. For the 40 trials for each transducer, eight values (groups) of packing density were tested, each consisting of five trials at the same packing density. Note, however, that in practice, since the ultrasound transducer's location and frequency will be fixed, the potential for human error due to switching will not exist.

The overall experimental arrangement is summarized in Table 2. The rated powder masses loaded into the tray for each group are listed in Table 3. The corresponding packing densities, calculated as the rated powder mass divided by the volume, are also provided in Table 3.

Table 2. Summary of experimental trials and the corresponding measurements made during each trial.

Trial numbers		**1-40**	**41-80**
Experiment stages	**Pre-recoating stage**	100 kHz acoustic-sensing pre-recoating measurements	200 kHz acoustic-sensing pre-recoating measurements
		Pre-recoating packing density measurements	
	Recoating stage	Force-sensing measurements	
	Post-recoating stage	100 kHz acoustic-sensing post-recoating measurements	200 kHz acoustic-sensing post-recoating measurements
		Post-recoating packing density measurements	

Table 3. Prescribed mass of powder loaded into the powder bed tray with the corresponding packing densities.

Group number	1	2	3	4	5	6	7	8
Rated mass loaded into container (g)	235	240	245	250	255	260	265	270
Rated packing density of powder	0.466	0.476	0.486	0.496	0.505	0.515	0.525	0.535

 doi:10.20944/preprints202604.1606.v1

3.5. Data Analysis

3.5.1. Data Analysis for Packing Density

The packing density for each trial was calculated based on the masses of powder measured. The powder bed was assumed to be uniformly packed both pre and post recoating.

The confined volumes before and after the recoating were 65097.85 mm^3 and 64738.19 mm^3, respectively. The density of 17-4PH stainless steel is 7.75 g/cm^3. Accordingly, each trial's pre- and post- packing densities (α_{pre} and α_{post}, respectively) were calculated based on their corresponding mass measurements m_{pre} and m_{post} as $\alpha_{pre} = m_{pre}/(65097.85\ mm^3 \times 7.75 \times 10^{-3}\ g/mm^3)$ and $\alpha_{post} = m_{post}/(64738.19\ mm^3 \times 7.75 \times 10^{-3}\ g/mm^3)$, respectively.

3.5.2. Data Analysis for Force-Sensing Method

Figure 9 shows an example force signal recorded in a trial of the experiment. With a recoating speed of 15 mm/s and a tray length of 100 mm, it takes approximately 6.7 s for the recoater to traverse the powder bed tray. The load cell detects small levels of reaction force while the recoater rolls over the tray's rims, as highlighted in the figure. When the recoater enters and exits the powder bed region, the force signal exhibits abrupt and inconsistent changes on the rim-powder interface. To minimize the influence of these transitions, a time window from 1600 ms to 5000 ms is chosen, as the time when the recoater is spreading the powder. Since the same travel speed and travel length are used for each trial, the specified time window roughly corresponds to the same locations on the powder bed for each trial.

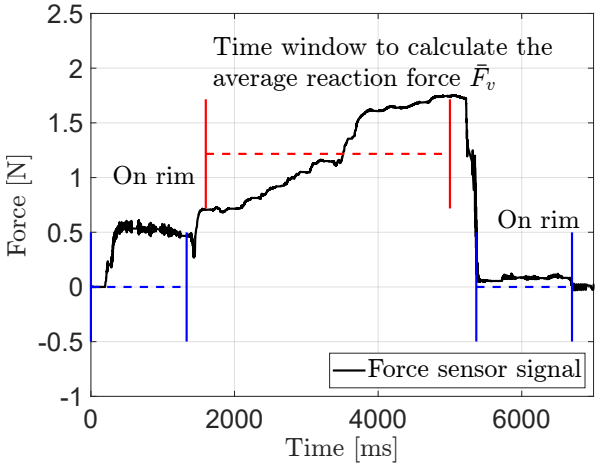

Figure 9. An example of reaction force signal collected from force-sensing apparatus.

The instantaneous recoating force (e.g., see Figure 9) reflects the local packing density at the corresponding location, which varies along the powder bed. However, the current setup lacks a method to directly measure the ground truth of the local packing density. Since this research is in an early-stage verification phase, for simplicity, we assume that the packing density is uniform across the powder bed. Therefore, the average vertical reaction force $\bar{F}_v$ measured within the aforementioned time window for each trial is treated as the output for the force-sensing method for that trial, and is correlated with packing density.

For curve fitting, Jenike and Shield [59] proposed a relationship between packing density α and the consolidating hydrostatic pressure σ, expressed as:

$$\alpha = \beta(1+\sigma)^{\gamma} \tag{4}$$

where β, γ are material-dependent parameters. At any given time, the consolidating hydrostatic pressure applied on the recoater can be considered to be linearly correlated with the reaction force, i.e., $\sigma = kF_v$, where k is a variable that is affected by how the powder bed deforms. If we assume that the deformations of the powder bed are consistent across all trials, then k remains constant across all trials,

 doi:10.20944/preprints202604.1606.v1

and $\bar{\sigma} = \bar{k}\bar{F}_v$, where $\bar{k}$ is a constant with an identical value for all trials. Substituting σ with $\bar{\sigma} = \bar{k}\bar{F}_v$ in Equation (4) yields Equation (5):

$$\bar{F}_v = p_1 \alpha^{p_2} - p_3 \tag{5}$$

which serves as our sensor model for fitting the experimental results. Here, p_1, p_2, and p_3 are the fitting parameters. The inverse of Equation (5), shown as Equation (6), maps the force measurement back to packing density.

$$\hat{\alpha}_f = \left(\frac{\bar{F}_v + p_3}{p_1} \right)^{1/p_2} \tag{6}$$

3.5.3. Data Analysis for Acoustic-Sensing Method

Figure 10 shows two examples of signals recorded with 100 kHz and 200 kHz ultrasound transducers. The initial pulses are the residual portions of the excitation signal. The second peaks are the first reflections from the powder bed. The subsequence signals are the echo signals due to reverberations from the ultrasound transducer and powder bed surfaces.

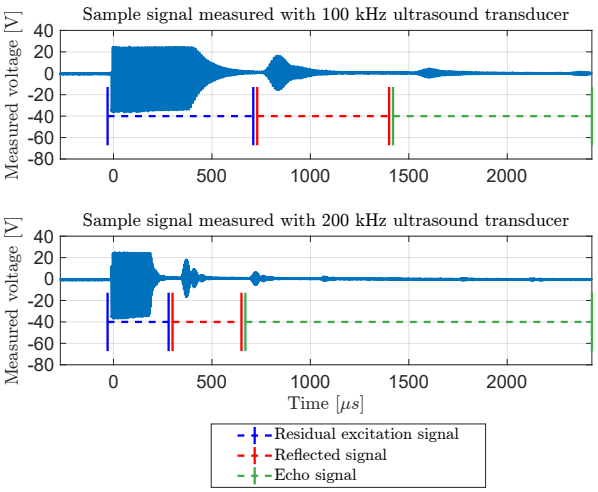

Figure 10. Examples of ultrasound signals collected from acoustic-sensing apparatus.

Time windows of 730 ¯s to 1400 ¯s, and 300 ¯s to 650 ¯s are chosen to extract the reflected signals from the 100 kHz and 200 kHz transducers, respectively. The signals are zero-centered by removing their offsets determined by taking the average of the last 500 samples in the time window for each signal, followed by a fast Fourier transform (FFT) to extract the amplitude spectrum of the reflected signal. Due to the manufacturing tolerances of ultrasound transducers and the system's error, the maximum amplitude is not perfectly located at the transducer's rated frequency. Instead, we treat the frequencies at maximum amplitudes of the FFT as the resonance frequencies of the corresponding transducers, and the maximum amplitudes are treated as the intensities of the reflected signals $I_{r,p}$. Figure 11 shows two examples of the measured signals, the extracted (and corrected) reflected signals, and the amplitude spectrum for the 100 kHz and 200 kHz transducers. The amplitude $I_{r,p}$ is treated as the output for the acoustic-sensing method.

 doi:10.20944/preprints202604.1606.v1

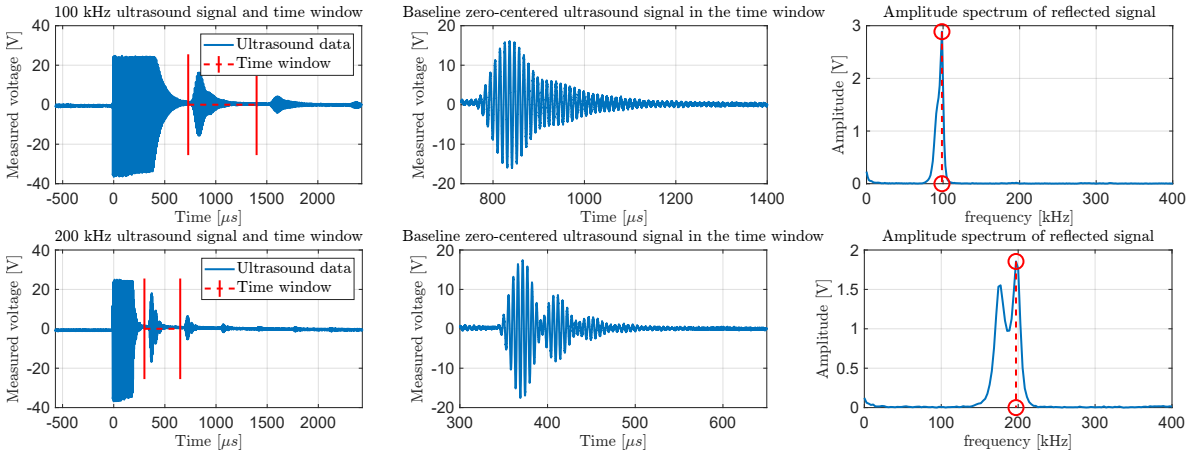

Figure 11. Examples of data collected with acoustic-sensing methods, with 100 kHz and 200 kHz ultrasound transducers.

A fitting model is proposed based on Equation (1). Since an ultrasonic transducer cannot measure its own emitted signal directly, the incident intensity I_i is unknown. However, the incident intensity is a constant across all trials with the same ultrasound transducer and can thus be treated as a fitting parameter. Rearranging Equation (1) yields Equation (7), which shows $I_{r,p}$ is a function that depends on powder's acoustic impedance Z_p:

$$I_{r,p} = I_i - \frac{2I_i Z_a}{Z_p + Z_a} \tag{7}$$

Coghill and Giang [54] found that, for glass powder, the packing density and sound's propagation speed c_p have a $1/6$ power law behavior. Based on this, an assumption is made that the sound propagation speed should still follow a power law, i.e., packing density α and powder acoustic impedance Z_p follow a correlation of Equation (8):

$$Z_p = q_1 \alpha^{q_2} \tag{8}$$

Substituting Equation (8) into Equation (7) yields the fitting model shown as Equation (9):

$$I_{r,p} = I_i - \frac{2I_i Z_a}{q_1 \alpha^{q_2} + Z_a} \tag{9}$$

Similarly, the inverse function shown as Equation (10) can be used to map the acoustic measurements back to the packing density.

$$\hat{\alpha}_{ac} = \left(\frac{2I_i Z_a}{q_1 (I_i - I_{r,p})} - \frac{Z_a}{q_1} \right)^{1/q_2} \tag{10}$$

Since I_i is constant for a given ultrasound transducer, the pre- and post-recoating measurements are merged into a single dataset for each transducer to determine its corresponding I_i value. For the 100 kHz and 200 kHz transducers, the fitted I_i values are 4.31 V and 2.35 V, respectively. Once I_i is determined, the parameters q_1 and q_2 are fitted using the separated datasets.

4. Results and Discussion

In the powder preparation process presented in Section 3.1, the cohesive forces of the powder cause some particles to stick to the leveling blade and press, resulting in minor discrepancies between the actual and desired powder masses in the powder tray. This causes discrepancies between the rated packing density (α_r) and the pre-recoating packing density (α_{pre}). This error is characterized and summarized in Figure 12 and Table 4. The difference between the rated and pre-recoating packing

 doi:10.20944/preprints202604.1606.v1

densities for each trial is below 0.60%, indicating that the pre-recoating packing densities are well controlled. Furthermore, Figure 12 shows the discrepancy between the rated packing density and post-recoating packing density α_{post} of the powder bed samples, assuming the powder bed is uniform after recoating. It is observed that, on average, packing density decreases after the recoating process and its discrepancy compared to α_r grows considerably. There are at least two factors contributing to this trend:

- Recoater – The recoater used in the current setup can be regarded as a fixed blade-type recoater, which does not provide excellent powder bed compaction [20,60]. Most commercial systems use an active roller to consolidate the powder more effectively.
- Powder bed inconsistency – Although the powder bed is assumed to be uniform, there may still be variations in packing density along the z-axis. The top portion of the powder bed may have a higher packing density than the bottom, as it is the first to come into contact with the press during the powder preparation process described in Section 3.1. Since the recoating process removes some powder from the top layer, it may remove the denser portion, resulting in the packing density decrements for the post-recoating samples.

Table 4. Powder mass loaded into the powder bed tray with their corresponding average errors and standard deviations.

Group number	1	2	3	4	5	6	7	8
Rated packing density of powder α_r	0.4658	0.4757	0.4856	0.4955	0.5054	0.5154	0.5253	0.5352
Average packing density error (%)	-0.177	-0.179	-0.200	-0.204	-0.237	-0.291	-0.307	-0.326
Standard deviation of packing density (%)	0.051	0.027	0.043	0.040	0.074	0.098	0.093	0.082

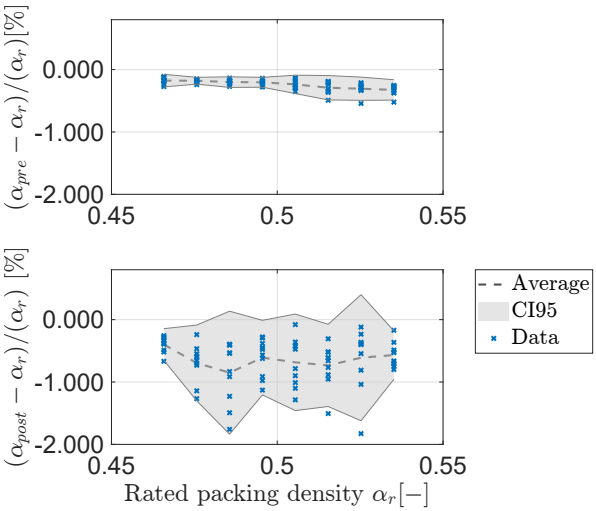

Figure 12. Deviation of actual packing density from rated values for pre-recoating and post-recoating powder beds.

Figure 13a,d show the average vertical reaction force $\bar{F}_v$ plotted against the corresponding pre- and post-recoating packing densities, respectively, based on data from the 80 experimental trials. The fitting function of Equation (5) is used to model the relationship between packing density and average vertical reaction force $\bar{F}_v$. The fitted curves, along with their R^2 values, are shown in Figure 13. Similarly, Figures 13b,c,e,f show the acoustic-sensing measurements versus the packing density for pre- and post-recoating powder beds, along with their fitted functions and corresponding R^2 values.

Using the fitted parameters, the inverse functions (Equations (6) and (10)) are employed to estimate the packing density $\hat{\alpha}$ from the sensor outputs. Figure 14 presents the percentage estimation

 doi:10.20944/preprints202604.1606.v1

errors: $(\hat{\alpha} - \alpha_{pre/post})/\alpha_{pre/post}$ along with the corresponding confidence intervals for each group of α_r. Table 5 summarizes the coefficient of determination (R^2) from the fitting, as well as the mean (μ) and standard deviation (s) of the estimation error, averaged across all eight α_r groups for each measurement condition.

Table 5. R^2 of the fitting, average μ and standard deviation s of the estimation error for each measurement case. For acoustic sensing cases, dedicated pre- and post-recoating measurements are compared with pre- and post-recoating packing densities. For force-sensing cases, the same data are compared with pre- and post-packing densities.

	Metric	**Force sensing**	**100** kHz **Acoustic-sensing**	**200** kHz **Acoustic-sensing**
Pre-recoating	μ	-0.0004	0.0007	0.0005
	s	0.0081	0.0215	0.0124
	R^2	0.8220	0.5343	0.7514
Post-recoating	μ	-0.0005	0.0003	0.0005
	s	0.0089	0.0125	0.0124
	R^2	0.8089	0.7906	0.7633

The force-sensing method has the highest R^2, lowest μ (with a minor exception) and lowest s among the three measurements. However, notice from Figure 14 that the fitting precision of the force sensor is superior at low values of α_r but deteriorates as α_r increases, for both the pre- and post-recoating cases. Three reasons may be responsible for this phenomenon. First, the utilization of a mallet for powder preparation (as discussed in Section 3.1) may introduce packing density inconsistencies in the powder bed in the vertical direction that are exacerbated at higher values of α_r. Second, the sensing model for the force sensor (Equation (6)) is nonlinear such that packing density errors are amplified at higher values of α. Third, the water-atomized powder (WAP) used in this study exhibits irregular particle morphology. At higher packing fractions, particle interlocking, aggregation, and cohesive interactions become more significant. Because the recoater in the current setup is stationary rather than rotating, it cannot effectively disrupt these agglomerates. During recoating, aggregated powder may adhere to the recoater surface, introducing force and post-recoating density fluctuations and increasing measurement variability across trials. Figure 16 shows the recoater surface after recoating for a representative trial in Group 8, where noticeable powder adhesion is observed. In contrast, only minimal powder adhesion is present in Group 1, indicating that this effect is associated with higher rated packing density. These three factors would explain why in Figure 14 larger confidence intervals are observed at higher values of α_r for the force sensor.

 doi:10.20944/preprints202604.1606.v1

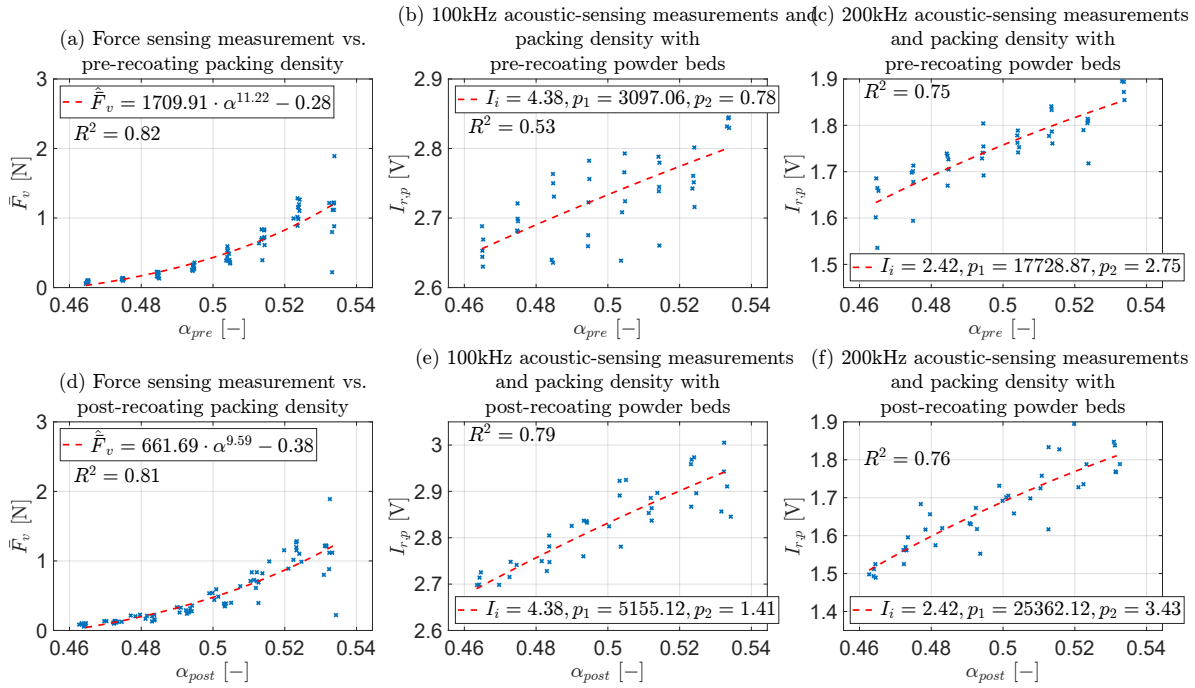

Figure 13. Sensing method outputs vs. pre- and post-recoating packing densities and their fitting results.

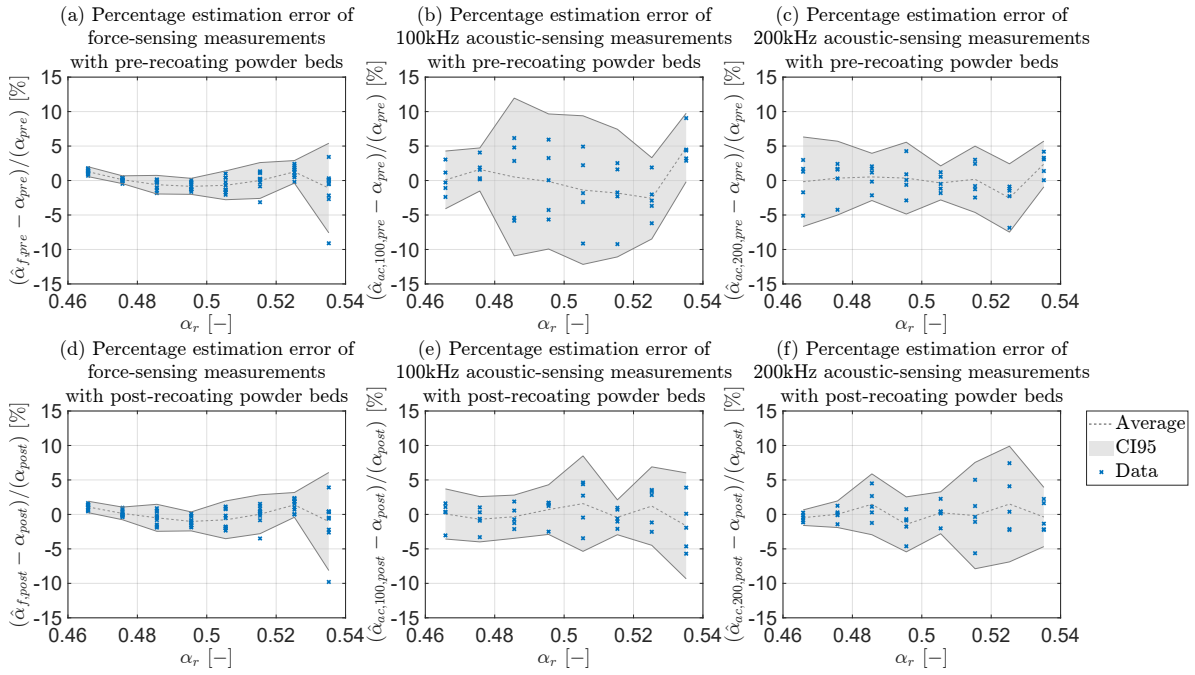

Figure 14. Estimation error for each measurement methods.

For the acoustic measurements, generally, the standard deviation s is larger than the force measurement. This may be due to the powder bed inhomogeneity. While the force sensor is averaging the force signal while the recoater is traversing on the powder bed, the inhomogeneity can be averaged. However, for the ultrasound transducer, since the measurements were taken at the center point of powder bed, the results might be affected by the inhomogeneity of the powder bed and show larger deviation. Meanwhile, the 200 kHz transducer outperforms the 100 kHz transducer in terms of R^2, μ and s in pre-recoating. However, in post-recoating, the 100 kHz transducer significantly improves its performance, matching or beating the 200 kHz transducer in all three metrics.

Figure 14 reveals some insights that may explain this observation. The 100 kHz acoustic-sensing measurements show relatively large confidence intervals between the α_r values of 0.47 and 0.51, while

 doi:10.20944/preprints202604.1606.v1

the confidence intervals on both extremes of α_r values are smaller. This confidence interval variation, along with the fitting quality improvement after recoating, for the 100 kHz acoustic measurements, can be attributed to the consolidation of powder. Ali. et al. show that, compared to free-flowing powder, sound has a higher impedance and faster propagation speed in caked powder [34]. To alter the packing density, the powder samples used in this study had to be consolidated as discussed in Section 3.1. The process of consolidation may produce a similar effect to that of caked powder and result in higher sound propagation speed for some frequencies. When the packing density is low, the lack of consolidation may consistently result in free-flowing powder, while higher packing densities may consistently lead to consolidated powder. However, for groups with intermediate packing densities, partial consolidation may inconsistently result in either free-flowing or consolidated powder, leading to the wide variability observed in the estimation of packing density in the intermediate ranges of α_r. Conversely, during recoating, the powder spreading process may disturb the consolidated powder and make the particles free-flowing post-recoating, yielding more consistent post-recoating measurements.

On the other hand, the 200 kHz measurements did not show such a significant difference between pre- and post-recoating estimates. A potential explanation lies in the difference in wavelengths of the transducers. The acoustic response of a powder bed is frequency-dependent. It is therefore possible that the 100 kHz transducer is more sensitive to the aforementioned caking effect, while 200 kHz acoustic waves may interact differently with the granular structure and be less affected by this effect. Further studies are required to explore the relationship between the acoustic response at different frequencies and the various conditions that affect the powder bed.

It is well known that the strengths of different sensors could be amplified and the weaknesses diminished through sensor fusion. As discussed above, the force sensor is more precise at lower values of packing density. Conversely, the acoustic sensors have much better precision at the highest values of packing density. Therefore, we sought to explore how the fusion of both types of sensors would perform. To do this, we utilized the corresponding estimations from the force-sensing method $\hat{\alpha}_f$ and the acoustic-sensing method $\hat{\alpha}_{ac}$ to compute a refined estimation $\hat{\alpha}_{fu}$ of packing density α. A constant-weighted fusion approach was adopted, expressed as:

$$\hat{\alpha}_{fu} = \eta_{fu}\hat{\alpha}_f + (1 - \eta_{fu})\hat{\alpha}_{ac} \tag{11}$$

Where η_{fu} is a constant weight. Four cases were evaluated:

- Force + 100 kHz acoustic-sensing (pre-recoating)
- Force + 200 kHz acoustic-sensing (pre-recoating)
- Force + 100 kHz acoustic-sensing (post-recoating)
- Force + 200 kHz acoustic-sensing (post-recoating)

The η_{fu} is determined independently for each case, by minimizing $\left|\hat{\alpha}_{fu} - \alpha_{pre/post}\right|$ over the corresponding datasets. The fusion parameters η_{fu} are summarized in Table 6. The standard deviation of the fusion estimation error, along with the average and standard deviation of estimation errors from individual methods, are summarized in Table 7 and Figure 15.

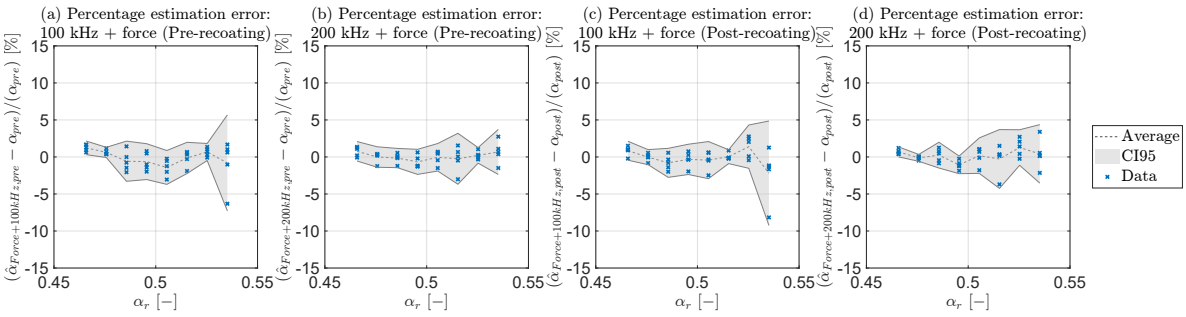

Figure 15. Estimation error for sensor fusion cases.

 doi:10.20944/preprints202604.1606.v1

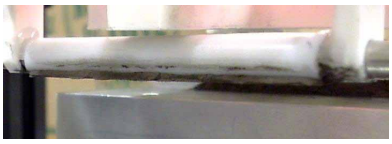

Recoater condition following the recoating process for Group 8 (rated packing density = 0.5352).

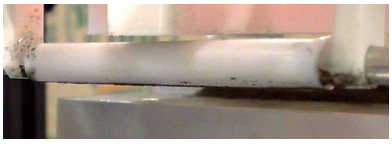

Recoater condition following the recoating process for Group 1 (rated packing density = 0.4658).

Figure 16. Recoater surface condition after recoating for low (Group 1) and high (Group 8) rated packing densities.

Table 6. η_{fu} for each cases.

Cases	**Jfu**
Force + 100 kHz acoustic-sensing (pre-recoating)	0.77
Force + 200 kHz acoustic-sensing (pre-recoating)	0.80
Force + 100 kHz acoustic-sensing (post-recoating)	0.60
Force + 200 kHz acoustic-sensing (post-recoating)	0.90

Since a constant-weighted fusion approach was adopted, the average estimation error of the fusion is expected to lie between the two individual measurements for each case. Notably, in all cases, the standard deviation of the estimation error decreased, indicating improved precision. This suggests that a combination of both types of sensor could be very beneficial.

Table 7. Mean and standard deviation of packing density estimation error for force, acoustic, and fusion sensing.

	Metric	Force-sensing (for 100 kHz Trials)	100 kHz Acoustic-sensing	Force-sensing (for 100 kHz Trials) + 100 kHz Acoustic-sensing	Force-sensing (for 200 kHz Trials)	200 kHz Acoustic-sensing	Force-sensing (for 200 kHz Trials) + 200 kHz Acoustic-sensing
Pre-recoating	μ	-0.0011	0.0007	**-0.0007**	0.0003	0.0005	**0.0004**
	s	0.0099	0.0215	**0.0080**	0.0060	0.0124	**0.0053**
Post-recoating	μ	-0.0018	0.0003	**-0.0010**	0.0009	0.0005	**0.0009**
	s	0.0105	0.0125	**0.0090**	0.0067	0.0124	**0.0066**

Despite its promising results, this study has some significant limitations. First, both detection methods lack systematic models that comprehensively incorporate various factors encountered in actual printing and accurately estimate the packing density based on sensor readings. For the force sensor, factors such as the presence of green parts [61], layer thickness [19], recoating speed [56], and the moisture level in the printer chamber can significantly affect the measured force; however, these parameters are not included in the currently adopted empirical model. For ultrasound sensing, the influence of other powder characteristics, such as tortuosity and permeability, on reflection behavior has not been systematically examined [62–64]. Second, both sensing methods have been tested only on dedicated setups, not in real printing environments. Meanwhile, due to the lack of measurement techniques for local packing densities, the powder bed is assumed to be uniform. Although the force sensing method reduces errors caused by powder bed inhomogeneity by averaging the force signal over the recoating path, the ultrasound measurement is obtained at a single location and is therefore more susceptible to local variations in packing density. In addition, under the assumption of a uniform powder bed, only the steady state responses of the sensors are evaluated, while their transient responses, that is, how quickly they can detect changes in packing density during actual printing, remain unclear. Third, the powder adhesion and aggregation observed on the recoater indicates the need for an actively driven roller configuration, which warrants further refinement of the experimental

 doi:10.20944/preprints202604.1606.v1

setup and operating procedure. Forth, although shear forces are partially mitigated by aligning the centerline of the recoater with that of the load cell, the shear distribution is not perfectly symmetric. As a result, residual shear components may still affect the measured force through torsional effects.

5. Conclusions and Future Work

This study investigated two promising approaches (recoating-force sensing and ultrasound-based acoustic sensing) for *in-situ* measurement of powder bed packing density in MBJ. Using a custom-built experimental setup, both sensing methods were evaluated over a range of packing densities using 17-4PH water-atomized stainless steel powder. Two ultrasonic transducers (100 kHz and 200 kHz) were tested in conjunction with a vertical recoating force sensor, and both the individual and combined sensor outputs were analyzed for estimation accuracy and precision.

Key findings of this study include:

1. *Force-Sensing Effectiveness:* The recoating force-sensing method demonstrated high correlation ($R^2 > 0.80$) with packing density in both pre- and post-recoating measurements. It also showed low average error and standard deviation, particularly in lower packing density ranges. However, its accuracy deteriorated slightly at higher densities, potentially due to inconsistencies in powder consolidation, powder aggregation and limitations of the current sensor model.
2. *Ultrasound-Based Acoustic Sensing:* The 200 kHz transducer outperformed the 100 kHz transducer in estimating pre-recoating packing density, achieving higher R^2 and lower standard deviation. However, after recoating, the 100 kHz transducer showed improved performance compared to pre-recoating, likely due to more consistent powder conditions following the spreading process. Variability in the 100 kHz measurements at mid-range densities suggests sensitivity to partial consolidation or caking effects.
3. *Sensor Fusion Advantage:* By combining force- and acoustic-sensing outputs using a constant-weighted fusion strategy, the standard deviation of estimation error was reduced relative to individual sensors, demonstrating the value of sensor fusion in enhancing robustness and confidence of packing density estimation.

Despite these promising results, several limitations remain. First, empirical models are adopted to directly relate data from both sensors to packing density; however, key process parameters and material characteristics are not considered. Second, the ex situ test apparatus and the assumption of a uniform powder bed not only adversely affect the ultrasound measurements, but also restrict the evaluation to the steady state responses of the sensors. Third, powder adhesion and aggregation is observed during the recoating process and introduces fluctuations in the recoating force measurements, particularly in high density groups. Fourth, shear forces may not be fully isolated from the recoating force measurements, and their influence requires further quantification and proper separation.

Future work will address these limitations by:

- *Modeling Enhancements for Force-sensing Method:* Developing improved force-sensing models that incorporate additional process parameters such as recoating velocity, blade geometry, powder type, layer thickness, moisture level, and interaction with green parts.
- *Physical Modeling Enhancement:* Develop comprehensive physical models for both sensor to accurately estimate the packing density based on the sensor signal and process parameters and material characteristics. For recoating-force sensor, the factors such as the presence of green parts [61], layer thickness [19], recoating speed [56] need to be included in the model. For airborne-ultrasound sensor, material properties such as tortuosity and permeability need to be modeled.
- *Testing Both Sensors in an In Situ Setup:* Both sensors will be evaluated in an in situ printing environment under actual binder jetting conditions. During printing, packing density is inherently established and subsequently preserved within the green parts, enabling localized density measurements that can be more directly correlated with sensor outputs compared to the uniform

 doi:10.20944/preprints202604.1606.v1

powder bed assumption. In addition, the dynamic response of the sensors and their capability to distinguish packing density variations during actual printing can be systematically assessed.

- *Improving the Recoating-Force Sensing Method:* An actively driven roller should be implemented, and shear forces must be systematically evaluated and properly isolated. These improvements are expected to better imitate the actual recoater behavior, enhance powder spreading performance by reducing the powder adhesion and aggregation's affect and improve the consistency and reliability of the force measurements.
- *Advanced Sensor Fusion Techniques:* Exploring physics informed machine learning approaches to more effectively integrate data from both sensors. For example, force sensing data may be used to infer material characteristics required for an accurate acoustic sensing model, thereby enhancing sensitivity and reducing estimation uncertainty.

This work lays the groundwork for robust in-situ monitoring of packing density in MBJ, an essential step toward process control and quality assurance in next-generation MBJ systems.

Author Contributions: Chen Qian – Writing – review & editing, Writing – original draft, Visualization, Validation, Methodology, Investigation, Formal analysis, Data curation, Conceptualization. Alexander Martinez-Marchese – Conceptualization, Investigation, Methodology, Software, Writing – review & editing. Chinedum Okwudire – Conceptualization, Methodology, Supervision,Writing – review & editing, Funding acquisition. All authors have read and agreed to the published version of the manuscript.

Funding: This project was partially supported by the T3N postdoctoral fellowship from the Michigan Economic Development Corporation.

Use of Artificial Intelligence: During the preparation of this work the author(s) used ChatGPT in order to check grammar errors and improve the language and readability of the manuscript. After using this tool/service, the author(s) reviewed and edited the content as needed and take(s) full responsibility for the content of the publication.

Acknowledgments: The authors would like to thank Dr. Kijoon Lee for his feedback on some of the preliminary work related to acoustic sensing.

Conflicts of Interest: The authors have filed a patent application [65] on the sensing methods described in this article.

References

1. Moghadasi, M.; Miao, G.; Li, M.; Pei, Z.; Ma, C. Combining powder bed compaction and nanopowders to improve density in ceramic binder jetting additive manufacturing. *Ceramics International* **2021**, *47*, 35348–35355. https://doi.org/https://doi.org/10.1016/j.ceramint.2021.09.077.
2. Zhao, K.; Su, Z.; Ye, Z.; Cao, W.; Pang, J.; Wang, X.; Wang, Z.; Xu, X.; Zhu, J. Review of the types, formation mechanisms, effects, and elimination methods of binder jetting 3D-printing defects. *Journal of Materials Research and Technology* **2023**, *27*, 5449–5469. https://doi.org/https://doi.org/10.1016/j.jmrt.2023.11.045.
3. Zhang, Y.; Wu, L.; Guo, X.; Kane, S.; Deng, Y.; Jung, Y.G.; Lee, J.H.; Zhang, J. Additive Manufacturing of Metallic Materials: A Review. *Journal of Materials Engineering and Performance* **2017**, *27*, 1–13. https://doi.org/10.1007/s11665-017-2747-y.
4. Gibson, I.; Rosen, D.; Stucker, B.; Khorasani, M., Binder Jetting. In *Additive Manufacturing Technologies*; Springer International Publishing: Cham, 2021; chapter 8, pp. 237–252. https://doi.org/10.1007/978-3-030-56127-7_8.
5. Sachs, E.; Cima, M.; Williams, P.; Brancazio, D.; Cornie, J. Three Dimensional Printing: Rapid tooling and prototypes directly from a CAD model. *Journal of Engineering for Industry* **1992**, *114*, 481–488. https://doi.org/10.1115/1.2900701.
6. Li, M.; Du, W.; Elwany, A.; Pei, Z.; Ma, C. Metal Binder Jetting Additive Manufacturing: A Literature Review. *Journal of Manufacturing Science and Engineering* **2020**, *142*, 090801. https://doi.org/10.1115/1.4047430.
7. Do, T.; Kwon, P.; Shin, C.S. Process development toward full-density stainless steel parts with binder jetting printing. *International Journal of Machine Tools and Manufacture* **2017**, *121*, 50–60. Special Issue on the State-of-the-Art in North American Manufacturing Research, https://doi.org/https://doi.org/10.1016/j.ijmachtools.2017.04.006.

 doi:10.20944/preprints202604.1606.v1

8. Markforged. Types of 3D printing in metal.
9. Do, T.; Shin, C.S.; Stetsko, D.; VanConant, G.; Vartanian, A.; Pei, S.; Kwon, P. Improving Structural Integrity with Boron-based Additives for 3D Printed 420 Stainless Steel. *Procedia Manufacturing* **2015**, *1*, 263–272. https://doi.org/10.1016/j.promfg.2015.09.019.
10. Bai, Y.; Williams, C.B. An exploration of binder jetting of copper. *Rapid Prototyping Journal* **2015**, *21*, 177–185. https://doi.org/10.1108/rpj-12-2014-0180.
11. Schmidt, J.; Parteli, E.J.; Uhlmann, N.; Wörlein, N.; Wirth, K.E.; Pöschel, T.; Peukert, W. Packings of micron-sized spherical particles – Insights from bulk density determination, X-ray microtomography and discrete element simulations. *Advanced Powder Technology* **2020**, *31*, 2293–2304. https://doi.org/https://doi.org/10.1016/j.apt.2020.03.018.
12. Mostafaei, A.; Elliott, A.M.; Barnes, J.E.; Li, F.; Tan, W.; Cramer, C.L.; Nandwana, P.; Chmielus, M. Binder jet 3D printing—Process parameters, materials, properties, modeling, and challenges. *Progress in Materials Science* **2021**, *119*, 100707. https://doi.org/https://doi.org/10.1016/j.pmatsci.2020.100707.
13. Ziaee, M.; Crane, N.B. Binder jetting: A review of process, materials, and methods. *Additive Manufacturing* **2019**, *28*, 781–801. https://doi.org/https://doi.org/10.1016/j.addma.2019.05.031.
14. Bai, Y.; Wagner, G.; Williams, C.B. Effect of Particle Size Distribution on Powder Packing and Sintering in Binder Jetting Additive Manufacturing of Metals. *Journal of Manufacturing Science and Engineering* **2017**, *139*, 081019, [https://asmedigitalcollection.asme.org/manufacturingscience/article-pdf/139/8/081019/6405404/manu_139_08_081019.pdf]. https://doi.org/10.1115/1.4036640.
15. Du, W.; Roa, J.; Hong, J.; Liu, Y.; Pei, Z.; Ma, C. Binder Jetting Additive Manufacturing: Effect of Particle Size Distribution on Density. *Journal of Manufacturing Science and Engineering* **2021**, *143*, 091002, [https://asmedigitalcollection.asme.org/manufacturingscience/article-pdf/143/9/091002/6733718/manu_143_9_091002.pdf]. https://doi.org/10.1115/1.4050306.
16. Yang, W.; Cai, Z.; Duan, W.; Deng, X.; Lin, T.; Chen, Z.; Xie, F.; Liu, J.; Qu, Z.; Jin, F.; et al. Effect of feedstock bimodal powder design and cold isostatic pressing on the mechanical behavior of binder jetting additive manufactured Inconel 718 superalloy. *Journal of Manufacturing Processes* **2025**, *133*, 607–622. https://doi.org/10.1016/j.jmapro.2024.11.085.
17. Chen, L.; Chen, W.; Zhang, S.; Zou, S.; Cheng, T.; Zhu, D. Effect of bimodal powder on densification and mechanical properties of 316L stainless steel fabricated by binder jet 3D printing. *Journal of Materials Research and Technology* **2023**, *27*, 4043–4052. https://doi.org/https://doi.org/10.1016/j.jmrt.2023.10.203.
18. Lee, Y.; Nandwana, P.; Simunovic, S. Powder spreading, densification, and part deformation in binder jetting additive manufacturing. *Progress in Additive Manufacturing* **2021**, *7*, 111–125. https://doi.org/10.1007/s40964-021-00214-1.
19. Barthel, B.; Janas, F.; Wieland, S. Powder condition and spreading parameter impact on green and sintered density in metal binder jetting. *Powder Metallurgy* **2021**, *64*, 378–386. https://doi.org/10.1080/00325899.2021.1912923.
20. Lee, S.J.J. Powder layer generation for three dimensional printing. PhD thesis, Massachusetts Institute of Technology, 1992.
21. Cao, S.; Qiu, Y.; Wei, X.F.; Zhang, H.H. Experimental and theoretical investigation on ultra-thin powder layering in three dimensional printing (3DP) by a novel double-smoothing mechanism. *Journal of Materials Processing Technology* **2015**, *220*, 231–242. https://doi.org/https://doi.org/10.1016/j.jmatprotec.2015.01.016.
22. Paudel, B.J.; To, A.C. Spatial green density variation and its effect on distortion prediction in binder jet additive manufacturing. *Additive Manufacturing* **2025**, *98*, 104640. https://doi.org/10.1016/j.addma.2025.104640.
23. Zheng, C.; Mostafaei, A.; de Vecchis, P.R.; Nettleship, I.; Chmielus, M. Microstructure evolution for isothermal sintering of binder jet 3D printed alloy 625 above and below the solidus temperature. *Additive Manufacturing* **2021**, *47*, 102276. https://doi.org/https://doi.org/10.1016/j.addma.2021.102276.
24. Parab, N.D.; Barnes, J.E.; Zhao, C.; Cunningham, R.W.; Fezzaa, K.; Rollett, A.D.; Sun, T. Real time observation of binder jetting printing process using high-speed X-ray imaging. *Scientific Reports* **2019**, *9*. https://doi.org/10.1038/s41598-019-38862-7.
25. Bidare, P.; Abdullah, R.; Jiménez, A.; Essa, K. Powder reusability in Metal Binder Jetting. *Proceedings of the Institution of Mechanical Engineers, Part E: Journal of Process Mechanical Engineering* **2023**, *238*, 1554–1560. https://doi.org/10.1177/09544089221147778.
26. Mirzababaei, S.; Paul, B.K.; Pasebani, S. Metal Powder Recyclability in Binder Jet Additive Manufacturing. *JOM* **2020**, *72*, 3070–3079. https://doi.org/10.1007/s11837-020-04258-6.

 doi:10.20944/preprints202604.1606.v1

27. Mostafaei, A.; Hughes, E.T.; Hilla, C.; Stevens, E.L.; Chmielus, M. Data on the densification during sintering of binder jet printed samples made from water- and gas-atomized alloy 625 powders. *Data in Brief* **2017**, *10*, 116–121. https://doi.org/10.1016/j.dib.2016.11.078.
28. Jiang, R.; Monteil, L.; Kimes, K.; Mostafaei, A.; Chmielus, M. Influence of powder type and binder saturation on binder jet 3D–printed and sintered Inconel 625 samples. *The International Journal of Advanced Manufacturing Technology* **2021**, *116*, 3827–3838. https://doi.org/10.1007/s00170-021-07496-3.
29. TAKAHASHI, T.; KINAI, Y.; OSADA, T.; KOBAYASHI, S. Effect of water atomized powder size on the flowability and sintered properties in metal binder jet 3D printing. *Mechanical Engineering Journal* **2023**, *10*, 22–00476–22–00476. https://doi.org/10.1299/mej.22-00476.
30. Elliott, A.M.; Nandwana, P.; Siddel, D.; Compton, B. A method for measuring powder bed density in binder jet additive manufacturing process and the powder feedstock characteristics influencing the powder bed density, 2016.
31. Miyanaji, H.; Rahman, K.M.; Da, M.; Williams, C.B. Effect of fine powder particles on quality of binder jetting parts. *Additive Manufacturing* **2020**, *36*, 101587. https://doi.org/https://doi.org/10.1016/j.addma.2020.101587.
32. Jacob, G.; Donmez, A.; Slotwinski, J.; Moylan, S. Measurement of powder bed density in powder bed fusion additive manufacturing processes. *Measurement Science and Technology* **2016**, *27*, 115601. https://doi.org/10.1088/0957-0233/27/11/115601.
33. Wischeropp, T.M.; Emmelmann, C.; Brandt, M.; Pateras, A. Measurement of actual powder layer height and packing density in a single layer in selective laser melting. *Additive Manufacturing* **2019**, *28*, 176–183. https://doi.org/https://doi.org/10.1016/j.addma.2019.04.019.
34. Ali, U.; Mahmoodkhani, Y.; Imani Shahabad, S.; Esmaeilizadeh, R.; Liravi, F.; Sheydaeian, E.; Huang, K.Y.; Marzbanrad, E.; Vlasea, M.; Toyserkani, E. On the measurement of relative powder-bed compaction density in powder-bed additive manufacturing processes. *Materials &; Design* **2018**, *155*, 495–501. https://doi.org/https://doi.org/10.1016/j.matdes.2018.06.030.
35. Mizutani, S.; Yamaguchi, D.; Fujiwara, T.; Yasumoto, M.; Kuroda, R. Real-time X-ray visualization of ink penetration into powder bed for binder jetting process. *NIP & Digital Fabrication Conference* **2018**, *34*, 162–162. https://doi.org/10.2352/ISSN.2169-4451.2018.34.162.
36. Lawrence, J.; Inkley, C.; Fezzaa, K.; Clark, S.J.; Crane, N.B. Observations of Binder Jetting Defect Formation Using High-Speed Synchrotron X-Ray Imaging. *2022 International Solid Freeform Fabrication Symposium*.
37. Inkley, C.G.; Lawrence, J.E.; Crane, N.B. Impact of controlled prewetting on part formation in binder jet additive manufacturing. *Additive Manufacturing* **2023**, *72*, 103619. https://doi.org/https://doi.org/10.1016/j.addma.2023.103619.
38. Chen, H.; Chen, Y.; Liu, Y.; Wei, Q.; Shi, Y.; Yan, W. Packing quality of powder layer during counter-rolling-type powder spreading process in additive manufacturing. *International Journal of Machine Tools and Manufacture* **2020**, *153*, 103553. https://doi.org/https://doi.org/10.1016/j.ijmachtools.2020.103553.
39. Barrett, C.; MacDonald, E.; Conner, B.; Persi, F. Micron-Level Layer-Wise Surface Profilometry to Detect Porosity Defects in Powder Bed Fusion of Inconel 718. *JOM* **2018**, *70*, 1844–1852. https://doi.org/10.1007/s11837-018-3025-7.
40. Tan Phuc, L.; Seita, M. A high-resolution and large field-of-view scanner for in-line characterization of powder bed defects during additive manufacturing. *Materials & Design* **2019**, *164*, 107562. https://doi.org/10.1016/j.matdes.2018.107562.
41. Brika, S.E.; Brailovski, V. A Novel Apparatus for the Simulation of Powder Spreading Procedures in Powder-Bed-Based Additive Manufacturing Processes: Design, Calibration, and Case Study. *Journal of Manufacturing and Materials Processing* **2023**, *7*. https://doi.org/10.3390/jmmp7040135.
42. Land, W.S.; Zhang, B.; Ziegert, J.; Davies, A. In-Situ Metrology System for Laser Powder Bed Fusion Additive Process. *Procedia Manufacturing* **2015**, *1*, 393–403. 43rd North American Manufacturing Research Conference, NAMRC 43, 8-12 June 2015, UNC Charlotte, North Carolina, United States, https://doi.org/https://doi.org/10.1016/j.promfg.2015.09.047.
43. Beitz, S.; Uerlich, R.; Bokelmann, T.; Diener, A.; Vietor, T.; Kwade, A. Influence of Powder Deposition on Powder Bed and Specimen Properties. *Materials* **2019**, *12*. https://doi.org/10.3390/ma12020297.
44. Mussatto, A.; Groarke, R.; O'Neill, A.; Obeidi, M.A.; Delaure, Y.; Brabazon, D. Influences of powder morphology and spreading parameters on the powder bed topography uniformity in powder bed fusion metal additive manufacturing. *Additive Manufacturing* **2021**, *38*, 101807. https://doi.org/https://doi.org/10.1016/j.addma.2020.101807.

 doi:10.20944/preprints202604.1606.v1

45. Lanzetta, M.; Sachs, E. Improved surface finish in 3D printing using bimodal powder distribution. *Rapid Prototyping Journal* **2003**, *9*, 157–166. https://doi.org/10.1108/13552540310477463.
46. Chen, H.; Zhao, Y.F. Process parameters optimization for improving surface quality and manufacturing accuracy of binder jetting additive manufacturing process. *Rapid Prototyping Journal* **2016**, *22*, 527–538. https://doi.org/10.1108/rpj-11-2014-0149.
47. Wang, S.; Crane, N.B. Noncontact measurement of density and thermal properties of SS 316L powder bed through flash thermography. *Rapid Prototyping Journal* **2024**, *30*, 1663–1674. https://doi.org/10.1108/rpj-01-2024-0049.
48. Liu, T.; Lough, C.S.; Sehhat, H.; Ren, Y.M.; Christofides, P.D.; Kinzel, E.C.; Leu, M.C. In-situ infrared thermographic inspection for local powder layer thickness measurement in laser powder bed fusion. *Additive Manufacturing* **2022**, *55*, 102873. https://doi.org/https://doi.org/10.1016/j.addma.2022.102873.
49. Liu, T.; Kinzel, E.C.; Leu, M.C. In-situ lock-in thermographic measurement of powder layer thermal diffusivity and thickness in laser powder bed fusion. *Additive Manufacturing* **2023**, *74*, 103726. https://doi.org/https://doi.org/10.1016/j.addma.2023.103726.
50. Liu, T.; Leu, M.C.; Kinzel, E.C.; Landers, R.G. 7 - In situ monitoring and feature extraction in laser powder bed fusion. In *Machine Learning for Powder-Based Metal Additive Manufacturing*; Singh, G.; Imani, F.; Tewari, A.; Mishra, S., Eds.; Additive Manufacturing Materials and Technologies, Elsevier, 2025; pp. 155–227. https://doi.org/https://doi.org/10.1016/B978-0-443-22145-3.00007-4.
51. Qian, C.; Wu, P.; Okwudire, C. Toward In-situ Sensing of Powder Packing Quality in Metal Binder Jetting Using Recoating Force. In Proceedings of the Proceedings of 53nd SME North American Manufacturing Research Conference (NAMRC 53), 2025.
52. Desktop Metal. TripleACT Powder Spreading System Overview. Technical report, Desktop Metal, Inc., 2022. White paper.
53. Al-Lashi, R.S.; Povey, M.J.W.; Watson, N.J. Ultrasonic wave propagation in powders. *J. Phys. Conf. Ser.* **2018**, *1017*, 012001. https://doi.org/10.1088/1742-6596/1017/1/012001.
54. Coghill, P.; Giang, P. Ultrasonic velocity measurements in powders and their relationship to strength in particles formed by agglomeration. *Powder Technology* **2011**, *208*, 694–701. https://doi.org/https://doi.org/10.1016/j.powtec.2010.11.040.
55. Brettell, J.M. Slowing of sound waves in powdered media. *Aust. J. Phys.* **1989**, *42*, 627. https://doi.org/10.1071/ph890627.
56. Miao, G.; Moghadasi, M.; Du, W.; Pei, Z.; Ma, C. Experimental investigation on the effect of roller traverse and rotation speeds on ceramic binder jetting additive manufacturing. *Journal of Manufacturing Processes* **2022**, *79*, 887–894. https://doi.org/10.1016/j.jmapro.2022.05.039.
57. Mostafaei, A.; Neelapu, S.H.V.R.; Kisailus, C.; Nath, L.M.; Jacobs, T.D.; Chmielus, M. Characterizing surface finish and fatigue behavior in binder-jet 3D-printed nickel-based superalloy 625. *Additive Manufacturing* **2018**, *24*, 200–209. https://doi.org/10.1016/j.addma.2018.09.012.
58. Botello, F.R.; Quintanilla, M.A.; Castellanos, A.; Grekova, E.F.; Tournat, V. Effect of the microstructure on the propagation velocity of ultrasound in magnetic powders. *Ultrasonics* **2018**, *82*, 153–160. https://doi.org/https://doi.org/10.1016/j.ultras.2017.07.021.
59. Jenike, A.W.; Shield, R.T. On the Plastic Flow of Coulomb Solids Beyond Original Failure. *Journal of Applied Mechanics* **1959**, *26*, 599–602. https://doi.org/10.1115/1.4012119.
60. Chen, Q.; Juste, E.; Lasgorceix, M.; Petit, F.; Leriche, A. Binder jetting process with ceramic powders: Influence of powder properties and printing parameters. *Open Ceramics* **2022**, *9*, 100218. https://doi.org/https://doi.org/10.1016/j.oceram.2022.100218.
61. Li, M.; Miao, G.; Du, W.; Pei, Z.; Ma, C. Difference between powder bed density and green density for a free-flowing powder in binder jetting additive manufacturing. *Journal of Manufacturing Processes* **2022**, *84*, 448–456. https://doi.org/10.1016/j.jmapro.2022.10.030.
62. Fellah, Z.E.A.; Berger, S.; Lauriks, W.; Depollier, C.; Trompette, P.; Chapelon, J.Y. Ultrasonic measurement of the porosity and tortuosity of air-saturated random packings of beads. *Journal of Applied Physics* **2003**, *93*, 9352–9359. https://doi.org/10.1063/1.1572191.
63. Fellah, Z.E.A.; Depollier, C. Transient acoustic wave propagation in rigid porous media: A time-domain approach. *The Journal of the Acoustical Society of America* **2000**, *107*, 683–688. https://doi.org/10.1121/1.428250.

 doi:10.20944/preprints202604.1606.v1

64. Allard, J.F.; Atalla, N. *Propagation of Sound in Porous Media: Modelling Sound Absorbing Materials*; Wiley, 2009. https://doi.org/10.1002/9780470747339.
65. Okwudire, C.; Lee, K.; Martinez, A.; Qian, C. Methods For Sensing Powder Packing Fraction In Powder-Bed Additive Manufacturing. US 63/794,011, 2025/4/24.